This article has been accepted for inclusion in a future issue of this journal. Content is final as presented, with the exception of pagination.

Study and Design of a Fast Start-Up Crystal Oscillator Using Precise Dithered Injection and Active Inductance

Alireza Karimi-Bidhendi, *Student Member, IEEE*, Haoran Pu, *Student Member, IEEE*, and Payam Heydari, *Fellow, IEEE*

***Abstract*— This paper presents a theoretical study and design of two techniques used to reduce start-up time (T_S) and energy (E_S) of Pierce crystal oscillator (XO). An analytical study of precise injection on a crystal resonator is introduced, and based on this paper, a relaxation oscillator with a dithered frequency is designed. Next, a study of negative resistance of XO's active circuitry and a method to boost its value beyond the limit set by a crystal static capacitor are presented. A gyrator-C active inductor with high linearity is developed to accelerate the start-up process by boosting the negative resistance. A prototype integrating these techniques is fabricated in a 180-nm CMOS process and shows a significant improvement compared with the prior art. Specifically, T_S and E_S are reduced by 102.7× and 2.9×, compared with the XO start-up with no assisting circuitry, to 18 μs and 114.5 nJ for a 48-MHz XO across a temperature range of −40 °C to 90 °C. The measured steady-state power and the phase noise of the XO are 180 μW and −135 dBc/Hz at 1-kHz offset.**

***Index Terms*— Active inductor (AI), gyrator-C, motional current, negative resistance, precise injection, quartz crystal, relaxation oscillator (RXO), start-up time, static capacitor.**

I. Introduction

The advent of emerging fields, such as body area networks for health care applications and massive wireless sensing for Internet of Things, demands ultra-low-power electronics to enhance the battery lifetime. A common method of reducing the power consumption, increasing the battery lifetime, and, thus eventually, enabling battery-less systems is to power cycle the whole system and operate in an intermittent fashion [1]–[3]. The wireless sensor nodes primarily constitute a transceiver for communication, an analog-to-digital converter for data conversion, and a back-end processing block, all required to be low power. Reference frequency synthesis, digital clock timebase, and the carrier frequency generations in these blocks are often realized using a crystal oscillator (XO) [4]. An XO commonly employs a Pierce structure, as shown in Fig. 1(a), due to its many advantages, such as low-power consumption, low component count, ease of design, and low phase noise. The start-up time T_S of an XO (few milliseconds for a megahertz (MHz) crystal) constitutes a bottleneck in the effectiveness and performance of power cycling schemes, either limiting the system latency or raising the standby power.

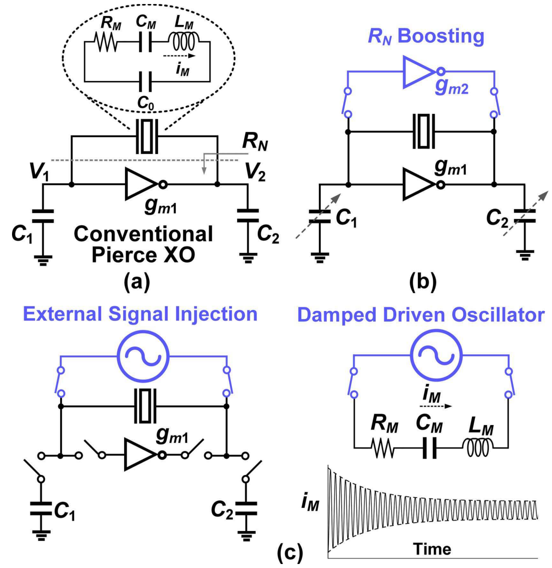

Fig. 1. (a) Pierce XO. (b) Boosting negative resistance by modifying capacitors and amplifier's gain. (c) Kick-starting the oscillator using an external periodic source and oscillation amplitude behavior under injection.

One approach to reduce standby power consumption overhead is to minimize the XO's power dissipation. In [5], a stacked amplifier was used as the XO's active network to increase the inverter's effective transconductance for a given bias current, thus lowering the power dissipation to 19 μW. Reference [6] implemented automatic self-power gating (ASPG) and multi-stage inverter for negative resistance (MINR) to intermittently power-off and reduce the short circuit current in the oscillator's inverter, thus lowering the power to as low as 9.2 μW. A more efficient way, which further decreases the sleep-mode power of the system, is to duty-cycle the XO and to allow it to be active only when needed. This approach, however, would need a mechanism to quickly start and stabilize the XO before the rest of the system is awakened. Therefore, techniques to reduce T_S with minimal energy overhead are of great interest.

Manuscript received February 8, 2019; revised April 10, 2019; accepted May 23, 2019. This paper was approved by Associate Editor Piero Malcovati. This work was supported by the National Science Foundation Frontier Award under Grant 1646275. *(Corresponding author: Alireza Karimi-Bidhendi.)*

The authors are with the Department of Electrical Engineering and Computer Science, University of California at Irvine, Irvine, CA 92697 USA (e-mail: akarimib@uci.edu; haoranp1@uci.edu; payam@uci.edu).

Color versions of one or more of the figures in this paper are available online at http://ieeexplore.ieee.org.

Digital Object Identifier 10.1109/JSSC.2019.2920084

A commonly used approach to lower T_S is shown in Fig. 1(b), which aims at increasing the active circuitry's negative resistance R_N by modifying the inverting amplifier's g_m or the capacitors C_1 and C_2. Reference [7] describes a method in which a minimum load capacitor C_L [defined as $C_L = C_0 + C_1C_2/(C_1+C_2)$] is applied to the oscillator during start-up, and once a stable oscillation is detected, a second capacitor bank is switched in to adjust the frequency and reach the desired steady state. Reference [8] implemented a similar concept to reduce T_S as well as start-up energy E_S by 13.3× and 6.9×, respectively, without the need to use a start-up sequence. However, this approach causes the oscillation frequency to be pulled away from the target, which results in an increase in T_S, defined as the time taken for XO to settle within a specified frequency error (e.g., ±20 ppm in [8]). Reference [9] presents two techniques to reduce T_S, namely, decreasing C_1/C_2 and increasing the current of the inverting amplifier during start-up. Another approach pursued by [10] and [11] is to increase C_L to enhance maximum achievable R_N. To be effective, this approach should be accompanied by increasing the amplifier's gain concurrently, which, in turn, increases E_S. If being implemented as a high-gain multi-stage circuit [6], [10], [12], the inverting amplifier can introduce a significant phase shift, which varies over process, voltage, and temperature (PVT). This phase shift may pull the XO frequency to even below the crystal's series resonance frequency ω_S so as to make the overall phase shift around the loop 360°, compromising the XO frequency stability and accuracy. Furthermore, under this condition, the crystal no longer behaves inductively and is forced to oscillate below the frequency that it is calibrated for. Due to this problem, [12] proposed to use two different amplifiers, one for start-up and another for steady-state operation.

Among several existing techniques, external signal injection is widely used to minimize T_S. For this technique to be effective though, the injected signal frequency should be close to the XO resonance frequency (e.g., within ±0.25%). Several implementations of this method have been proposed, each with various degrees of success. Reference [13] proposes a calibration system where proper frequency setting for a tunable oscillator is determined to help quickly start the XO by precise signal injection. A similar method was presented in [14], where a ring oscillator with a calibration circuitry injects a precise signal to reduce T_S of a 32-MHz Pierce XO to 50 μs. Reference [15] introduced a dithering technique to compensate for the frequency variations over process and temperature and reduced T_S of a 24-MHz XO to 64 μs. For a PVT-robust injection, [16] proposed a chirp injection (CI) mechanism to sweep the injection frequency around the crystal's resonance frequency. Another CI technique was proposed in [12] to reduce the area occupied by the chirp signal generator. To improve the signal injection accuracy, [17] proposed a three-step initialization sequence. In the first step, a coarsely tuned (±0.5% frequency accuracy) ring oscillator increases the XO amplitude to 0.2 V. In the second step, a phase-locked loop (PLL) aligns the ring oscillator frequency to within 20 ppm of the XO resonance frequency and, finally, applies the injection again in the last step. T_S is reduced to 19 μs, a 31.5× improvement compared with a normal start-up condition. In order to continuously drive the crystal with an external oscillator, [18] proposed a synchronized signal injection technique. Since there is a frequency offset between the injection signal and the crystal resonance, the phase difference between the two accumulates over time, which results in the injection signal counteracting the crystal resonance. The underlying idea in [18] is to realign the phase of the injection signal and the crystal resonance periodically to avoid this phase accumulation. For a 0.75-V steady-state differential amplitude (0.37 V single-ended), $T_S = 23$ μs and $E_S = 20.2$ nJ. A precisely timed injection method was presented in [19], and an analysis was provided to determine the optimum duration of injection. It also implemented a voltage regulation loop to limit the oscillation amplitude to ≈0.2 V (at the cost of higher phase noise) and achieved a T_S value of 2 μs. Such small amplitude can easily be built-up through a signal injection over a short time. Furthermore, the regulation loop itself assists the oscillation by providing a larger bias current during the start-up transient and a smaller one in the steady state.

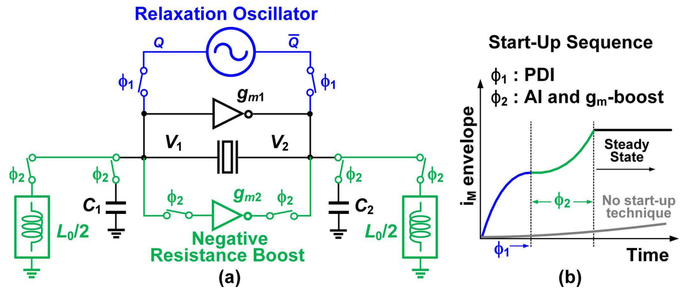

Fig. 2. (a) Proposed implementation of the fast-starting XO. (b) Oscillation amplitude growth with the start-up aids and without them.

II. Background and the Proposed Ideas

It is well known that the envelope of the XO motional current i_M is a direct indication of the oscillation behavior. In this paper, a rigorous study of signal injection for XO T_S reduction is presented, and the conditions leading to an optimal start-up behavior are derived. It will be proven that precise injection with exactly the same frequency as the crystal's series resonance frequency provides the fastest oscillation start-up. It will also be shown that, in reality, due to non-zero injection frequency inaccuracy, this mechanism alone cannot energize the crystal to skip the regenerative process interval. Therefore, another mechanism is needed to minimize this interval and thus lower T_S close to its theoretical lower limit.

In this paper, two techniques are proposed to realize this thought process. Fig. 2(a) shows the schematic of the proposed ideas, namely a relaxation oscillator (RXO) as an injection signal source and an active inductor (AI). The initialization start-up sequence and a symbolic behavior of oscillation amplitude growth are shown in Fig. 2(b). In the first phase ϕ_1 of the start-up sequence, RXO rapidly increases the oscillation amplitude, equivalent to an increase of the start-up initial condition for the XO. In the second phase ϕ_2, RXO is detached, while the AI, C_1, C_2, and an additional amplifier are switched in. In the

This article has been accepted for inclusion in a future issue of this journal. Content is final as presented, with the exception of pagination.

steady state, only C_1 and C_2 will remain connected to sustain the oscillation.

To be able to achieve a significant reduction in T_S and E_S, a deep understanding of the fundamentals of crystal and XO operation is necessary.

The rest of this paper is organized as follows. Section III presents a transient analysis in the presence of a periodic injection signal and studies parameters affecting T_S. It also covers the design and implementation of the RXO. Section IV illustrates the AI method to boost R_N and elaborates the design tradeoffs and considerations for robust operation of the AI leading to the improvement of the XO start-up time. Section V discusses the measurements of the fabricated XO and its start-up assisting circuitry, and finally, Section VI concludes this paper.

III. Precise Dithered Signal Injection

Consider Fig. 1(c), demonstrating an external signal injection mechanism for a Pierce XO and i_M behavior under injection. A differential periodic square signal is generated by an external oscillator (e.g., a ring or an RC oscillator) and then is buffered and applied to the crystal. Since a crystal resonator exhibits ultra-high quality factor ($\sim 10^6$) and very narrow bandwidth, it heavily attenuates any applied signal with frequencies not matching its resonance frequency. Thus, only the fundamental component is considered in the Fourier series expansion of the applied signal, while any phase noise around this tone is omitted. We assume that zero initial conditions for crystal only analyze the forced response to a periodic square signal applied at time $t = 0$. This is a valid assumption since, in practice, the initial condition is determined by the oscillator thermal noise. Non-zero initial conditions just complicate the analysis without adding much circuit insights.

A. Problem Statement: Damped Driven Oscillator

The characteristic differential equation for a crystal resonator excited by a periodic voltage source (i.e., damped driven oscillator), as shown in Fig. 1(c), for $t \geq 0$ is

$$v(t) = \frac{4V_{\text{DD}}}{\pi}\sin\omega_{\text{inj}}t = L_M\frac{di_M}{dt} + R_M i_M + \frac{1}{C_M}\int_0^t i_M d\tau \tag{1}$$

where ω_{inj} is the injection frequency. L_M, R_M, and C_M are the motional inductor, resistor, and capacitor of the crystal, respectively. With zero initial conditions, taking the derivative of (1) results in

$$\frac{4V_{\text{DD}}\omega_{\text{inj}}}{\pi L_M}\cos\omega_{\text{inj}}t = \frac{d^2 i_M}{dt^2} + 2\alpha\frac{di_M}{dt} + \omega_S^2 i_M \tag{2}$$

where $\alpha = R_M/2L_M$ and $\omega_S = 1/\sqrt{L_M C_M}$. Taking the Laplace transform and then using its convolution property, i_M is derived as

$$i_M(t) = \frac{4V_{\text{DD}}\omega_{\text{inj}}}{\pi L_M\omega_d}\int_0^t e^{-\alpha(t-x)}\sin\omega_d(t-x)\cos\omega_{\text{inj}}x\ dx \tag{3}$$

where $\omega_d = (\omega_S^2 - \alpha^2)^{1/2}$ is the damped natural frequency. Note that for crystal resonators, $\alpha \ll \omega_S$, and hence, $\omega_d \simeq \omega_S$. Using trigonometric identities, the integration in (3) is expanded, that is

$$\begin{aligned} i_M(t) &= \frac{2V_{\text{DD}}\omega_{\text{inj}}}{\pi L_M\omega_d}e^{-\alpha t}\sin\omega_d t \\ &\times\left[\int_0^t e^{\alpha x}\cos(\omega_d-\omega_{\text{inj}})x\ dx - \int_0^t e^{\alpha x}\cos(\omega_d+\omega_{\text{inj}})x\ dx\right] \\ &- \frac{2V_{\text{DD}}\omega_{\text{inj}}}{\pi L_M\omega_d}e^{-\alpha t}\cos\omega_d t \\ &\times\left[\int_0^t e^{\alpha x}\sin(\omega_d-\omega_{\text{inj}})x\ dx - \int_0^t e^{\alpha x}\sin(\omega_d+\omega_{\text{inj}})x\ dx\right]. \end{aligned} \tag{4}$$

The integrals in (4) with sum frequency components $\omega_d + \omega_{\text{inj}}$ are contributing negligibly to $i_M(t)$ and are thus ignored. If evaluated for an ideal case of $\omega_d = \omega_{\text{inj}}$ for which the crystal amplitude undergoes its fastest growth, (5) is readily derived

$$i_M(t) \simeq i_{M,\text{env}}(t)\sin\omega_d t \tag{5}$$

where $i_{M,\text{env}}(t)$ denotes the envelope of $i_M(t)$ and is calculated to be

$$i_{M,\text{env}}(t) = \frac{2V_{\text{DD}}}{\pi L_M\alpha}(1-e^{-\alpha t}) = \frac{4V_{\text{DD}}}{\pi R_M}(1-e^{-\alpha t}). \tag{6}$$

T_S is defined as the time when $i_{M,\text{env}}(t) = 0.9|I_{M,\text{SS}}|$, where $I_{M,\text{SS}}$ is the steady-state magnitude of i_M. It has been shown that at this time instance, the oscillation frequency has also settled within the required accuracy for most communication standards [16], [19]. The minimum achievable start-up time $T_{S,\min}$ in the XO is thus obtained from (6) and is equal to

$$T_{S,\min} = \frac{2L_M}{R_M}\ln\left(1 - \frac{\pi R_M}{4V_{\text{DD}}}\times 0.9|I_{M,\text{SS}}|\right)^{-1}. \tag{7}$$

It is instructive to acquire a quantitative insight into $T_{S,\min}$ using (7) for the widely used Pierce XO. As demonstrated in [20], in steady state

$$|I_{M,\text{SS}}| \simeq 0.5\left(1 + \frac{C_0}{C_S}\right)\omega_{\text{osc}}C_1|V_1| \tag{8}$$

where $\omega_{\text{osc}} = \omega_S(1 + C_M/2C_L)$ is the oscillation frequency, V_1 denotes the input voltage of the inverting amplifier, and C_S is the series combination of C_1 and C_2 in Fig. 1(a). For a sample 48-MHz crystal with parameters $C_M = 4$ fF, $L_M = 2.749$ mH, $R_M = 15\ \Omega$, $C_L = 8$ pF, $C_0 = 2$ pF, and $|V_1| = V_{\text{DD}}$, $T_{S,\min}$ is calculated to be 11.9 μs.

Now, assuming an injection frequency inaccuracy of $\Delta\omega = \omega_d - \omega_{\text{inj}}$, $i_M(t)$ becomes

$$\begin{aligned} i_M(t) = &\frac{2V_{\text{DD}}\omega_{\text{inj}}}{\pi L_M\omega_d(\alpha^2+\Delta\omega^2)}\sin\omega_d t \\ &\times[\alpha\cos\Delta\omega t + \Delta\omega\sin\Delta\omega t - \alpha e^{-\alpha t}] \\ &- \frac{2V_{\text{DD}}\omega_{\text{inj}}}{\pi L_M\omega_d(\alpha^2+\Delta\omega^2)}\cos\omega_d t \\ &\times[\alpha\sin\Delta\omega t - \Delta\omega\cos\Delta\omega t + \Delta\omega e^{-\alpha t}]. \end{aligned} \tag{9}$$

In practice, even for an integrated oscillator carefully designed to produce a precise injection frequency, it is still difficult for

ω_{inj} to be within $\pm 0.1\%$ of ω_d across PVT variations (e.g., for typical crystals operating in the MHz range, $\alpha \sim$ 1–10 kHz, while $\Delta\omega \sim$ 0.1–1 Mrad/s); hence, $\alpha \ll \Delta\omega$. Therefore, the expression in (9) is reduced to

$$i_M(t) \simeq \frac{2V_{\text{DD}}}{\pi L_M \Delta\omega}\left(1 - \frac{\Delta\omega}{\omega_d}\right)[\sin\omega_d t \sin\Delta\omega t + \cos\omega_d t(\cos\Delta\omega t - e^{-\alpha t})]. \quad (10)$$

B. Analysis of the Motional Current's Envelope

To calculate the envelope of $i_M(t)$ in (10), Hilbert transform is invoked. For an arbitrary waveform $\upsilon(t)$, a complex signal $z(t) = \upsilon(t) + j\hat{\upsilon}(t)$ is defined, where

$$\hat{\upsilon}(t) \equiv H[\upsilon(t)] = \upsilon(t) * \frac{1}{t} = \frac{1}{\pi}\int_{-\infty}^{\infty} \frac{\upsilon(\lambda)}{t - \lambda} d\lambda \quad (11)$$

is the Hilbert transform of $\upsilon(t)$. It is proved that the magnitude of $z(t)$ is the envelope of $\upsilon(t)$, i.e., $\upsilon_{\text{env}}(t) = |z(t)| = (\upsilon^2(t) + \hat{\upsilon}^2(t))^{1/2}$. For clarity, (10) is rewritten as

$$i_M(t) = K[x(t)\cos\omega_d t + y(t)\sin\omega_d t] \quad (12)$$

where

$$K = \frac{2V_{\text{DD}}}{\pi L_M \Delta\omega}\left(1 - \frac{\Delta\omega}{\omega_d}\right)$$
$$x(t) = \cos\Delta\omega t - e^{-\alpha t}, \quad y(t) = \sin\Delta\omega t. \quad (13)$$

$\hat{i}_M(t)$ is derived as

$$\hat{i}_M(t) = K[x(t)\sin\omega_d t - y(t)\cos\omega_d t]. \quad (14)$$

The envelope of $i_M(t)$ is, thus, readily calculated from (12) and (14)

$$i_{M,\text{env}}(t) = K\sqrt{x^2(t) + y^2(t)} = \frac{2V_{\text{DD}}}{\pi L_M \Delta\omega}\left(1 - \frac{\Delta\omega}{\omega_d}\right) \times \sqrt{1 + e^{-2\alpha t} - 2\cos\Delta\omega t\ e^{-\alpha t}}. \quad (15)$$

A consequence of the condition $\alpha \ll \Delta\omega$ is that it is unlikely that the injection oscillator alone can build up the oscillation amplitude of the Pierce XO all the way to its steady state, unless the steady-state amplitude is made small (e.g., $<0.2V_{\text{DD}}$, as was done in [19] and [21]). Therefore, $i_{M,\text{env}}(t)$ after injection is smaller than $I_{M,\text{SS}}$, and other techniques need to complement the signal injection, as was carried out by [16] and [22]. Following the excitation period, the crystal is detached from the external source and connected to the inverting amplifier.

Fig. 3 compares the time-domain variation of $i_{M,\text{env}}(t)$ obtained from both simulation and calculation [see (15)] of the crystal resonator under injection for two values of $\Delta\omega = 0.1, 0.3$ Mrad/s, validating the proposed analysis. For comparison, the $i_{M,\text{env}}(t)$ variation with injection time obtained from analysis in [19] (for the same circuit conditions and the same crystal model) is overlaid in Fig. 3. Reference [19] approximates the frequency response of crystal with an impulse function, only a valid approximation for small T_{inj}. On the contrary, the proposed dynamic analysis of the crystal's motional current is based on the characteristic differential equation of the crystal with no assumption about its frequency- and/or time-domain responses.

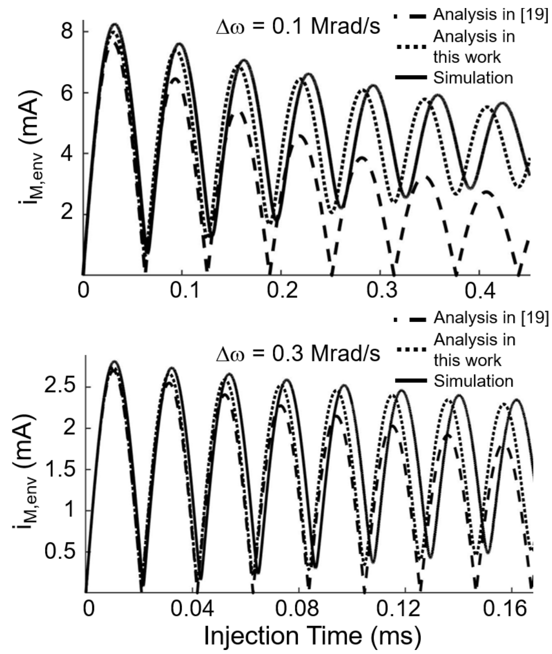

Fig. 3. Envelope of i_M for $\Delta\omega = 0.1$ and 0.3 Mrad/s.

For T_S to get sufficiently close to $T_{S,\text{min}}$, the injection should cease when $i_{M,\text{env}}(t)$ in (15) is at its maximum (see Fig. 3). This optimum injection time T_{OPT} is calculated to be $T_{\text{OPT}} \simeq \pi/\Delta\omega$. Moreover, the maximum of $i_{M,\text{env}}(t)$ is

$$i_{M,\text{env}}(t)_{\max} \simeq \frac{4V_{\text{DD}}}{\pi L_M \Delta\omega}\left(1 - \frac{\Delta\omega}{\omega_d}\right). \quad (16)$$

It is inferred that for crystals with high Q-factors or injection sources with poor frequency accuracy, $i_{M,\text{env}}(t)$ assumes smaller values for $t \le T_{\text{OPT}}$, an intuitively expected result.

In the case that injection oscillator's frequency is close to ω_d, it can be readily proved that so long as $\Delta\omega < (4C_M/\pi C_L)\omega_{\text{osc}}$, the injection mechanism alone is capable of bringing the oscillation amplitude to its steady state.

C. Sensitivity to Timing and Injection Frequency Inaccuracies

It was shown in Section III-B that injection should be stopped once $i_{M,\text{env}}$ reaches its peak value to minimize T_S. Two phenomena affect T_S, namely, inaccurate injection frequency ($\Delta\omega$) and time (T_{inj}). Recall that $i_{M,\text{env}}(t)$ exhibits a damped sinusoidal characteristic, as shown in Fig. 3. Thus, at the time, when $i_{M,\text{env}}(t)$ is at maximum, its time-derivative is at minimum, which in turn lowers the impact of injection duration inaccuracy on T_S. This is in contrast with the injection approach in [19], where the injection is stopped before the envelope reaches its maximum. In case the oscillation amplitude has not reached its steady state at the end of injection period, it will grow exponentially by the amplifier

$$i_M(t) = i_{M,\text{env}}(T_{\text{inj}})e^{(t - T_{\text{inj}})/\tau}u(t - T_{\text{inj}}), \quad \tau = \frac{-2L_M}{R_M + R_N} \quad (17)$$

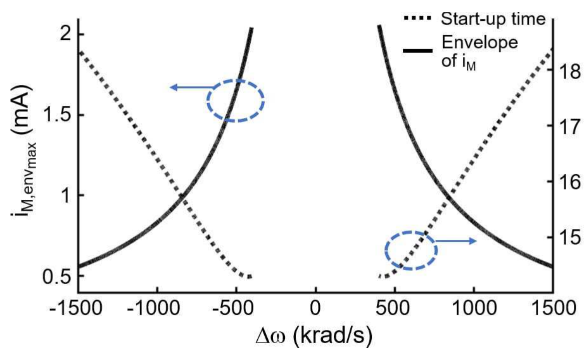

Fig. 4. Effect of injection frequency inaccuracy on a maximum value of $i_{M,\mathrm{env}}$ and overall T_S, given injection stops at $t = T_{\mathrm{OPT}}$ and $R_N = 50R_M$.

where $u(t)$ is the unit step function. To derive a closed-form expression for T_S, we assume that the amplifier remains linear and retains a constant R_N as the amplitude grows. Combining (8) and (17) yields

$$T_A = \tau \ln \frac{0.9(C_S + C_0)\omega_{\mathrm{osc}} V_{\mathrm{DD}}}{i_{M,\mathrm{env}}(T_{\mathrm{inj}})}, \quad T_S = T_{\mathrm{inj}} + T_A \tag{18}$$

where T_A is the time taken for the amplitude to grow toward its steady state after injection. Combining (16) and (18), the effect of $\Delta\omega$ on T_S is calculated as follows:

$$T_S \simeq \frac{\pi}{|\Delta\omega|} + \tau \ln[0.7 L_M (C_S + C_0)\omega_{\mathrm{osc}}|\Delta\omega|]. \tag{19}$$

Fig. 4 demonstrates the sensitivity of T_S to $\Delta\omega$ for the sample 48-MHz quartz crystal based on the quantitative evaluation of (16) and (19). Evaluating the effect of each term of (19) on T_S, if $\Delta\omega$ or crystal's Q-factor is small, the first term will be dominant. On the other hand, as the oscillation amplitude becomes large, the active circuitry becomes nonlinear. Therefore, τ starts to get larger, and the second term in (19) may dominate T_S. Similarly, larger Q-factors also increase the contribution of the second term on T_S. To reduce the effect of $\Delta\omega$ on T_S, one can lower τ to reduce T_S and its sensitivity to inaccurate frequency errors.

To evaluate the sensitivity of T_S to injection duration errors, the injection oscillator is assumed to be sufficiently precise, such that $\Delta\omega$ falls within $\pm 0.15\%$ of ω_d. The frequency of this oscillator is measured and, if required, calibrated before applying to the XO. Based on (15) and (18), Fig. 5 shows the variation of T_S with $\Delta\omega$ for four distinct injection times. For injection frequency errors less than 600 krad/s, T_S varies from 14.4 to 20.4 μs, as T_{inj} increases from 5 to 8 μs. In practice, the phase-noise-induced frequency skirts around ω_{inj} pump larger energy within the crystal bandwidth compared with an ideal single-tone injection. As will be illustrated in Section III-E, this can be achieved through dithering, thus resulting in lower T_S variation. Moreover, as will be seen in Section IV, this sensitivity is further reduced by introducing an AI to the circuit to significantly lower τ.

D. Interpretation of the Analysis

From the aforementioned equations, a number of observations are made as follows:

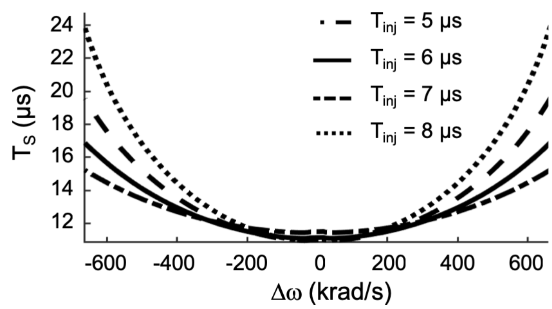

Fig. 5. Effect of injection timing inaccuracy on overall T_S for the sample crystal parameters. R_N is assumed to be $50R_M$.

1) $i_{M,\mathrm{env}}(t)_{\max}$ can reach twice the final value under continuous injection (steady-state value).
2) A smaller $\Delta\omega$ value results in larger $i_{M,\mathrm{env}}(t)_{\max}$, T_{OPT}, and $i_{M,\mathrm{env}}(t)$ during the start-up interval $0 < t < T_{\mathrm{OPT}}$.
3) To the first order, T_{OPT} is only a function of injection signal accuracy and not the crystal properties. In actual implementations, $\Delta\omega$ is larger for crystals with higher operating frequencies. This is because it becomes increasingly more difficult to guarantee the accuracy of an integrated oscillator as frequency rises.
4) It can also be shown that smaller $\Delta\omega$ value leads to larger local minimums for $i_{M,\mathrm{env}}(t)$, an effect not predicted in [19] (see Fig. 3).

E. Relaxation Oscillator Implementation

Among various candidates to create injection signal, ring oscillators have been used extensively, providing features, such as fast turn-on time, small area and power dissipation at the cost of large PVT susceptibility, and low-frequency precision. Alternatively, this paper employs an RXO, which provides a more precise injection, as its frequency depends on an easily tunable RC time constant instead of transistor parameters. A modified version of the architecture in [23] is implemented at 48 MHz while maintaining the performance across PVT (see Fig. 6). To account for the crystal's ultra-high Q, the RXO frequency ω_{inj} is modulated by toggling its capacitance C_2 between 400 and 415 fF through an internal feedback, as shown in Fig. 6. Thus, ω_{inj} alters by $\pm 0.25\%$, slightly spreading the injection signal power spectrum over a wider frequency range and raising the phase noise. This ensures that the RXO contains enough energy across the crystal bandwidth to limit T_S variation over temperature, resulting in a robust start-up behavior. As opposed to [15] where a relatively inaccurate ring oscillator was used, higher frequency accuracy of RXO allows for a lower dithering range of $\pm 0.25\%$. To reduce RXO frequency variation due to PVT, reference voltage V_{ref} is generated by a resistive voltage division ratio. Series poly and diffusion resistors with complementary temperature coefficients are employed to generate V_{ref}, thereby compensating for the RXO frequency variation due to temperature across process corners [23]. These resistors employ 5 bits of coarse and 4 bits of fine-tuning, which translates to a frequency resolution of 40 kHz and a tuning range from 27 to 84 MHz. Due to several percentage-point variations

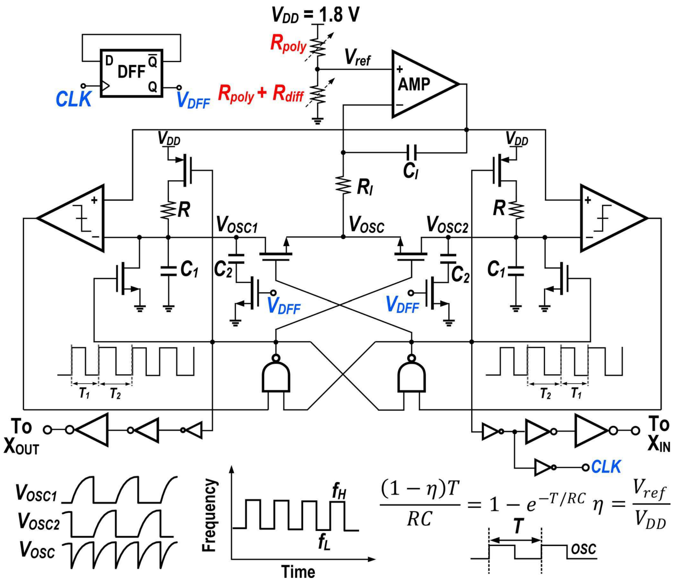

Fig. 6. RXO circuit implementation.

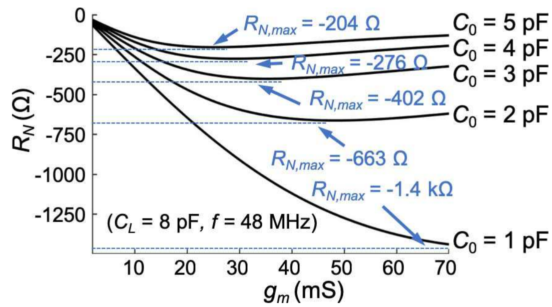

Fig. 7. Negative resistance and its maximum versus amplifier transconductance gain for various C_0 values.

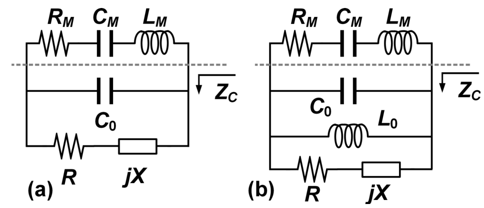

Fig. 8. One-port linear model of the XOs in (a) [12] and (b) this paper.

of on-chip resistors and capacitors, a simulation-assisted initial calibration is inevitable for any signal injection technique including the proposed precise dithered injection (PDI) (except for the chirp signal injection where the frequency is swept across a wide range). Measurement of this RXO shows frequency variation within ±0.15% over −40 °C to 90 °C, significantly better than temperature-compensated ring oscillators. Simulations show ±0.2% frequency variation across temperature at different process corners. Furthermore, Monte Carlo simulations of both process and mismatch variations show a sigma of 100 kHz (0.21%) in the nominal corner. The RXO and the buffer dissipate 3.6 mW from a 1.8-V supply, a significantly larger value compared with [23] because of higher operation frequency and more stringent specification on its frequency stability, which requires smaller comparators' delays. The power would be significantly lower on an advanced technology node or for smaller target frequency.

IV. Active Inductor

A. Effects of C_0 on XO Start-Up

The presence of the static capacitance C_0 in the crystal greatly influences the XO behavior [see Fig. 1(a)]. Besides limiting the pull-ability of XO, it lowers the active circuitry's negative resistance according to [20]

$$R_N = \frac{-4g_m C_S^2}{(g_m C_0)^2 + 16\omega^2 C_S^2 C_L^2}. \tag{20}$$

Furthermore, it limits the maximum negative resistance $R_{N,\max}$ and sets an optimum value of amplifier's g_m beyond which R_N will start to decrease (see Fig. 7)

$$R_{N,\max} = \frac{1}{2\omega C_0(1 + C_0/C_S)}, \quad g_{m,\mathrm{opt}} = 4C_S\omega(1 + C_S/C_0). \tag{21}$$

In addition, C_0 poses a limit on how much C_L can be lowered to achieve larger R_N [8], [24]. To address the limitation imposed by C_0, [12] proposed a dual-mode g_m scheme, employing one amplifier for start-up (A_{XO-3}) and another one for steady-state (A_{XO-1}) operation. A_{XO-3} is designed to show an inductive reactance X around the XO nominal operation frequency to counteract C_0. Starting with Fig. 8(a) that shows a linear model of the XO, the impedance Z_C seen from the motional branch is derived as

$$Z_C = \frac{R + j\left(X(1 - C_0X\omega) - R^2C_0\omega\right)}{(1 - C_0X\omega)^2 + (RC_0\omega)^2}. \tag{22}$$

In a conventional design, $X = -1/C_S\omega$, and crystal's motional branch is loaded with $C_S + C_0$. On the other hand, maximizing the real part of Z_C for the circuit model in Fig. 8(a) leads to $X = 1/C_0\omega$, while its imaginary part becomes $-1/C_0\omega$. Therefore, during start-up, when A_{XO-3} is enabled to boost the negative resistance, crystal's motional branch is effectively loaded with an equivalent capacitor of C_0, and ω_{osc} will shift toward ω_p. This frequency drift along with the nonlinearity effects of A_{XO-3} which was pointed out in [12] increases both amplitude and frequency settling times.

B. Proposed R_N Boosting Method

Fig. 8(b) shows a simplified linear model for the approach presented in this paper. An inductor is explicitly placed in parallel with the crystal to maximize the real part of Z_C for the circuit model in Fig. 8(b). Crystal's motional branch is now loaded with

$$Z_C = \frac{Z_{\mathrm{amp}}L_0s}{L_0s + Z_{\mathrm{amp}}(1 + L_0C_0s^2)}, \quad Z_{\mathrm{amp}} = R + jX \tag{23}$$

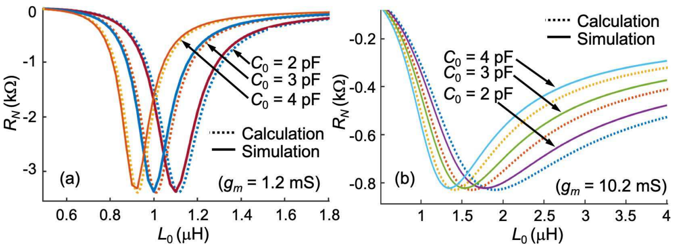

Fig. 9. R_N at 48 MHz after addition of L_0 for amplifier's transconductance gain of (a) 1.2 and (b) 10.2 mS.

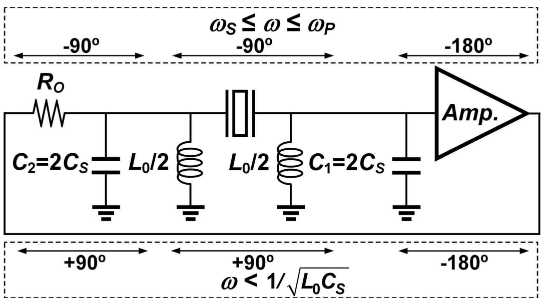

Fig. 10. Simplified phase shift around the loop of Pierce XO at different frequency ranges.

with real and imaginary parts expressed as

$$\mathrm{Re}\{Z_C\} = \frac{RL_0^2\omega^2}{R^2(1-L_0C_0\omega^2)^2+\big(L_0\omega+X(1-L_0C_0\omega^2)\big)^2} \tag{24}$$

$$\mathrm{Im}\{Z_C\} = \frac{R^2L_0\omega(1-L_0C_0\omega^2)+XL_0\omega\big(L_0\omega+X(1-L_0C_0\omega^2)\big)}{R^2(1-L_0C_0\omega^2)^2+\big(L_0\omega+X(1-L_0C_0\omega^2)\big)^2}. \tag{25}$$

L_0 boosts the real part of Z_C, and in contrast to [22], this can be accomplished without imposing any constraints on C_S value or amplifier's characteristic. More precisely, L_0 reduces the effective static capacitance $C_{0,\mathrm{eff}} = C_0[(\omega_0/\omega)^2 - 1]$ (where $\omega_0 = 1/(L_0C_0)^{1/2}$), thereby increasing $R_{N,\max}$. One may choose to leverage this property to decrease C_S so as to achieve larger R_N.

Fig. 9(a) and (b) demonstrates both simulated and calculated R_N variations with respect to L_0 under three values of C_0 (i.e., 2, 3, and 4 pF) and for two g_m values (i.e., 1.2 and 10.2 mS) at 48 MHz, where L_0 is assumed to be an ideal inductor. As shown in Fig. 9(a) and (b), the maximum achievable R_N value is larger for an amplifier with a lower g_m value. It is also observed that this larger R_N value requires more precise and linear L_0 over PVT variations, which is challenging to realize in practice. Therefore, to reduce the R_N sensitivity to L_0 variation, g_m should be increased [see Fig. 9(b)].

C. Design Considerations for Active Inductor Implementation

The addition of L_0 creates the possibility of an unwanted oscillation caused by the resonance through L_0, the crystal, and the amplifier. A qualitative view is displayed in Fig. 10. The AI is decomposed into two equal parts placed on the crystal's input and output nodes. For the oscillation to take place, the phase shift across the loop should be $n\times 360°$, where n is an integer number. Neglecting the AI first, one can identify a 180° phase lag from the amplifier, a phase lag of about 90° from $R_O - C_2$, and another 90° phase lag from the crystal$-C_1$ at $\omega_{\mathrm{osc}} = \omega_S$, where R_O is the amplifier output resistance. On the other hand, in the presence of AIs, the resulting passive network and the crystal form a dual-resonance network with two oscillation modes. Besides the oscillation mode at $\omega_{\mathrm{osc}} = \omega_S$, the second oscillation mode is created by the 90° phase leads associated with R_O–L_0 and crystal$-L_0$ and a 180° phase lag from the amplifier. With sufficient gain, the loop may, in fact, oscillate at this parasitic mode. One solution to suppress this mode is to decrease AI's Q-factor; an easily achievable task as the AI's Q-factor is inherently lower than that of monolithic or off-chip components. For better illustration, Fig. 11 shows the open-loop (from the amplifier's output to its input) gain and phase shift simulation of the dual-resonance network for two Q-factors.

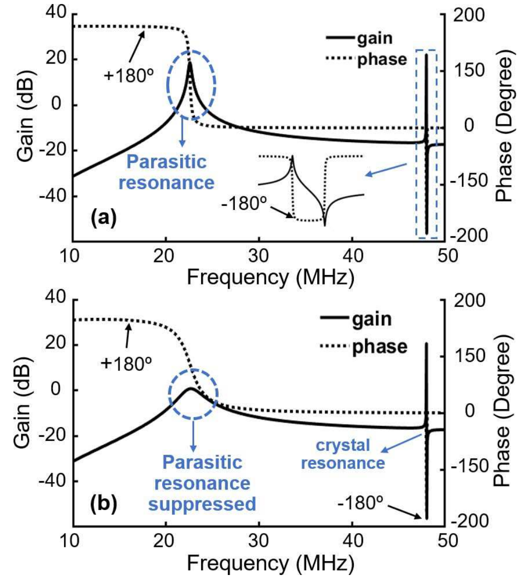

Fig. 11. (a) Tank frequency response after inclusion of L_0 with a quality factor of (a) 83 and (b) 11.

The AI's Q-factor cannot be arbitrarily low because it will increase the XO resistive loss. As a secondary measure to ensure the XO oscillation in its desired mode without compromising on the AI's Q-factor, the injection mechanism raises the XO initial condition around ω_S to a value substantially larger than the one provided by thermal noise to the unwanted mode. Once the desired operation takes over, the unwanted mode is automatically eliminated. Another issue is the possibility of operation at one of the crystal's overtones. To prevent this problem, notice that for the feedback to remain positive and oscillation to take place, the reactances at the crystal's input and output in Fig. 10 should be of the same sign (e.g., both negative) at the oscillation frequency of interest. Thus, placing half of L_0 on both sides of the XO guarantees this condition to satisfy at the fundamental frequency.

Finally, when it comes to the XO circuit design, comprehensive transient and spectral simulations have been performed

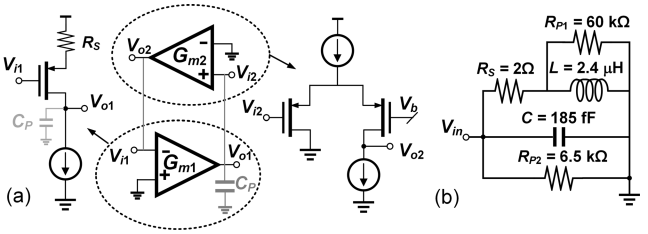

Fig. 12. AI implementation concept. (a) Constructing positive and negative transconductances. (b) Approximate model of the actual design.

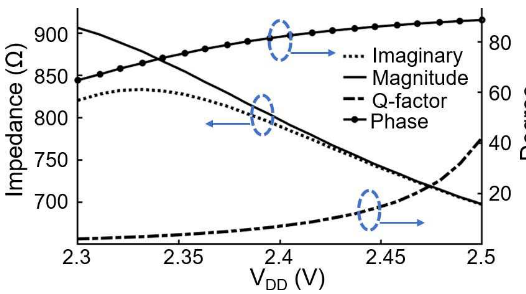

Fig. 13. AI input impedance characteristics at 48 MHz across supply.

to account for all the nonidealities (e.g., amplifier gain and bandwidth, nonlinearity, and frequency response of AI).

D. Circuit Implementation

Fig. 12(a) shows the building blocks of the gyrator-C AI. The negative transconductance is a degenerated common-source stage, and the positive one is a source-coupled structure. These blocks provide large input and output impedances, thereby increasing the Q-factor of the AI. Source degeneration reduces the dependence of G_{m1} on the input level, reduces the voltage gain at the output (to keep the transistors in saturation), and improves linearity as well as sensitivity to supply variation. Fig. 13 shows the input impedance of AI at 48 MHz and the corresponding Q-factor variations versus V_{DD}. The reactance varies by $\pm 9\%$ from 2.3 to 2.5 V, roughly translating to the same variation in the effective inductance. Reduced G_{m1} value has to be compensated for by increasing G_{m2}, which leads to higher power consumption (a bias current of 1.5 mA for G_{m2} cell). Cascode current sources are used for biasing to increase the Q-factor of the structure. The pMOS transistors are used to provide the higher input voltage range since AI and XO are dc-coupled. As shown in Fig. 14, the AI schematic is comprised of two single-ended structures operating at 2.4-V supply to accommodate stacked transistors and maintain constant transconductance values (and effective inductance) over a large signal swing. A combination of proportional to absolute temperature (PTAT) and constant-g_m current sources with 1.5- and 1-μA tuning resolutions, respectively, is used to bias M_1 with a nominal bias current of 14 μA, tune the effective inductance value, and reduce its variation across PVT. The AI operates over a wide frequency range (i.e., up to its self-resonance frequency), virtually accommodating all MHz crystals. The AI is notorious for being noisy and, thus, is usually used in applications

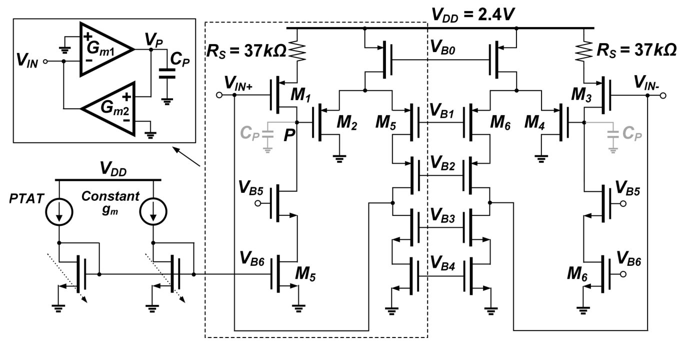

Fig. 14. AI circuit schematic.

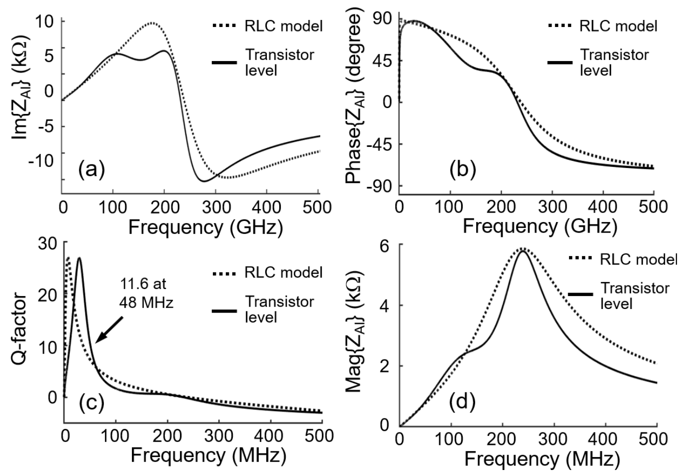

Fig. 15. AI reactance versus frequency and its equivalent circuit model.

with relaxed noise requirements. Nonetheless, for the intended purpose of the XO start-up improvement in this paper, the AI's noise, indeed, helps in reducing T_S.

Fig. 12(b) shows the synthesized equivalent RLC model for the proposed AI. The equivalent RLC components are readily derived by equating the input impedances of this model and the AI circuit in Fig. 14, that is

$$L \simeq \frac{C_P}{G_{m1}G_{m2}},\ R_{P2} = R_{o2},\ R_S = \frac{1}{G_{m1}G_{m2}R_{o1}},\ C = C_{in}$$
$$R_{P1} = \frac{R_{o1}}{1+g_{m1}R_S},\ G_{m1} = \frac{g_{m1}}{1+g_{m1}R_S},\ G_{m2} = \frac{g_{m2}}{2} \tag{26}$$

where C_P (R_{o1}) and C_{in} (R_{o2}) are the capacitances (resistances) at the drain and gate of M_1, respectively. Fig. 15 shows and compares the frequency response and Q-factor of the AI and its RLC model. The AI has multiple poles, which causes the two responses to deviate at high frequencies. However, the model is sufficiently accurate up to $\sim$0.1 GHz. Fig. 16 shows the simulation results for the negative resistance and its associated boosting ratio across temperature after the addition of the AI. The R_N values in Fig. 16 are estimated from the rate of oscillation amplitude growth in large-signal transient simulations. These values are smaller in magnitude than the ones predicted in Fig. 9 because of the AI nonlinearity, namely, variation of G_{m1} and G_{m2} with signal swing. For a given C_0, the AI maintains a relatively constant R_N ($<\pm 9\%$ worst-case variation for $C_0 = 2$ pF)

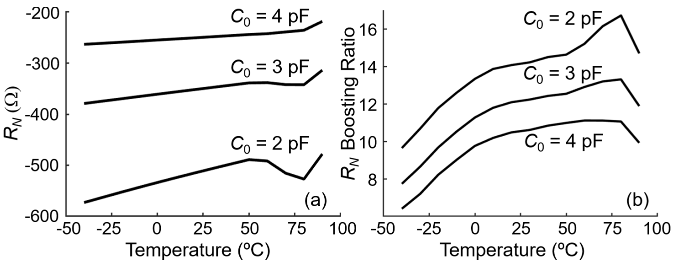

Fig. 16. Simulated temperature variations of (a) R_N after addition of the AI and (b) R_N boosting ratio.

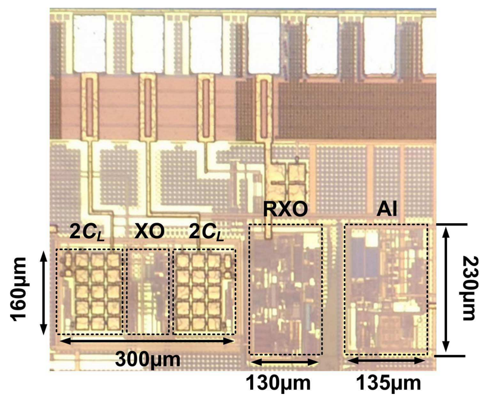

Fig. 17. Die micrograph of the prototype.

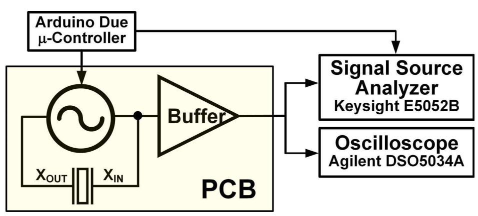

Fig. 18. Measurement setup.

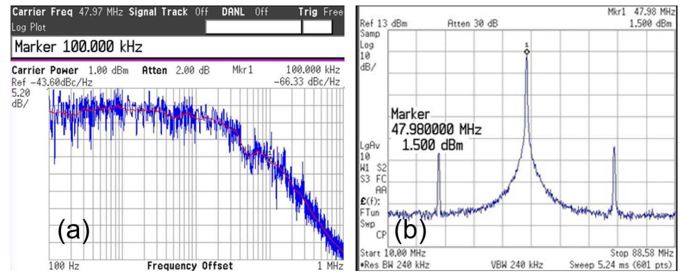

Fig. 19. (a) Measured RXO phase noise and (b) power spectral density.

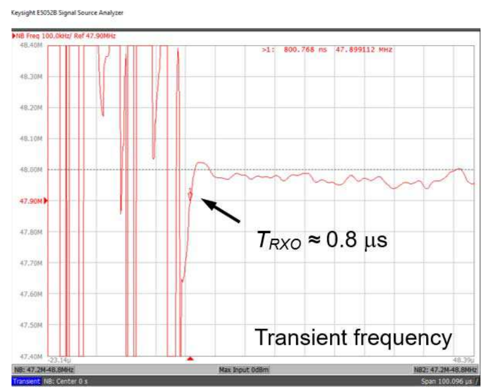

Fig. 20. RXO start-up time.

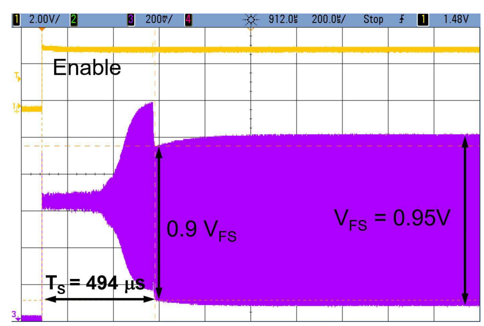

Fig. 21. T_S improvement using AI only for a large steady-state oscillation amplitude of 0.95 V.

across a −40 °C to 90 °C temperature range, which, thus, keeps the T_S variations small.

To lower T_S for crystals with large C_0 values, the duration of the second phase ϕ_2 of the start-up sequence in Fig. 2 should increase. According to the simulations of motional current amplitude in the nominal process corner and at room temperature, T_S increases from 17 to 22 μs for C_0 varying from 1 to 6 pF (for the same unloaded crystal Q-factor). The optimal value of ϕ_2 can be found using two methods: (1) measuring crystal's R_M and C_0 and using simulations to find the optimum duration and (2) using an oscillation amplitude detection circuitry to disable ϕ_2 when the near-steady-state amplitude is reached. Signal injection duration ϕ_1 is independent of C_0 since T_{OPT} only depends on $\Delta\omega$.

V. Measurement Results

Fig. 17 shows the die micrograph of the chip fabricated in a 180-nm CMOS process. Occupying an active area of 0.108 mm^2, this chip integrated on-chip capacitors including a capacitor bank to create the equivalent 8-pF C_L. It was wire bonded into a quad-flat no-leads (QFN) package and mounted on an FR-4 PCB. Operating at 48 MHz, the oscillator employs a surface-mount crystal with a 3.2×2.5 mm^2 package size and dissipates 180 μW from a 1-V supply (generated through a low dropout regulator) at steady state. The supply of 1 V was chosen for ease of comparison with prior work. The steady-state power is mainly determined by the supply voltage, operation frequency, C_L, oscillation amplitude, and crystal properties. It can be minimized through circuit techniques such as stacked-amplifier architecture in [5]; however, this was not the focus of this paper.

The measurement setup is shown in Fig. 18. An off-chip buffer was used to monitor the signal on X_{IN}, and a micro-controller generates the start-up sequence. The RXO phase noise and the power spectral density are shown in Fig. 19. The RXO phase noise was purposely increased to −66 dBc/Hz at 100-kHz offset through dithering. The two spurs in the RXO's power spectrum are due to the fact that the RXO output is the sum of two half-wave rectified signals. The measured RXO frequency settles within 0.8 μs, as shown in Fig. 20, which is dominated by the RXO's integrator pole $R_I C_I$ in Fig. 6. Although this start-up time is larger than

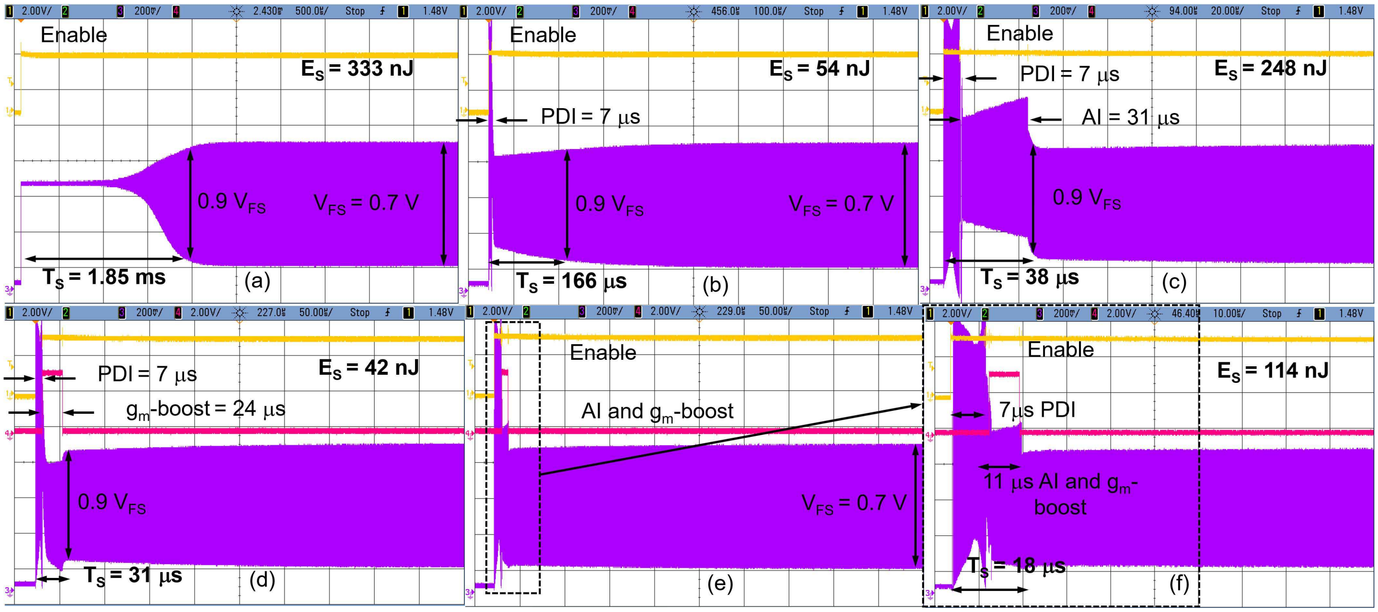

Fig. 22. Start-up behavior of XO with (a) no kick-start technique, (b) PDI only, (c) PDI and AI techniques, (d) PDI and g_m-boost, and (e) and (f) all techniques combined.

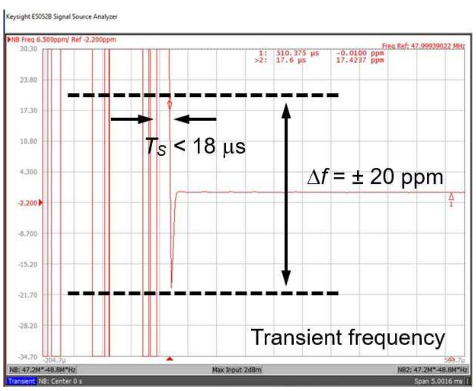

Fig. 23. Settling of XO oscillation frequency.

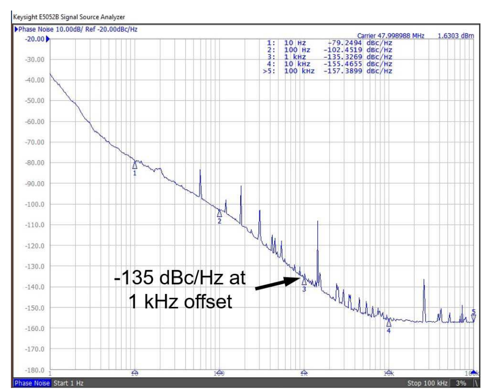

Fig. 24. Measured phase noise.

that of a ring oscillator, it is still negligible compared with the XO's T_S. Therefore, the accurate and stable frequency provided by the RXO justifies its usage.

Fig. 21 shows the measured voltage at X_{IN}, demonstrating the oscillation start-up behavior using the AI only. The XO supply is increased to 1.5 V with a steady-state oscillation voltage of 0.95 V and $T_S = 3.96$ ms without the AI. Even at this large voltage swing, the AI is able to reduce T_S to 0.494 ms, an 8× improvement ratio.

Fig. 22(a)–(f) shows the strobed voltage X_{IN} to evaluate T_S and E_S using different techniques. In the absence of any start-up assistant technique, T_S and E_S of the XO were measured to be 1.85 ms and 333 nJ, respectively. The RXO frequency was calibrated using the trimming poly and diffusion resistors (see Fig. 6), and the injection time is fixed at 7 μs. Using the PDI technique, T_S and E_S were improved by 11.1× and 6.2× to 166 μs and 54 nJ, respectively. Enabling the PDI and the AI without increasing the amplifier's g_m (i.e., using the same g_m value as in the steady state), T_S was reduced to 38 μs, inferring ≈5× boosting of R_N. Applying PDI and rising the amplifier's g_m (g_m-boost) by switching in g_{m2} [see Fig. 2(a)], T_S was reduced to 31 μs with a slight decrease in E_S compared with using PDI only. Combining all techniques, T_S and E_S were further reduced by 102.7× to 18 μs and 2.9× to 114.5 nJ, respectively, compared with the case where no techniques were utilized. The start-up time has been significantly improved compared with prior work that boosts negative resistance (see [8] and [12]), albeit with higher E_S. In systems where latency is of concern or power dissipation during their active period is large, minimizing the start-up time is considered to be the main objective function. The increased E_S value is due to high power consumption associated with the AI and g_m-boosting techniques. Measured power consumption (estimated E_S) for AI, RXO (including buffers), and amplifiers g_{m1} and g_{m2} [see Fig. 2(a)] is 7.2 mW (79 nJ), 3.6 mW (27 nJ), and 0.5 mW (8 nJ), respectively. According to the transient simulations of the XO start-up behavior, hypothetically, if AI is removed and the R_N-boost amplifier g_{m2} is scaled in size and power by an additional factor of 12 and 3, $T_S \simeq 22$ μs and $E_S \simeq 124$ nJ. The measured T_S value varies by 2% for a 25% variation in the injection time and by ±12% over a temperature range of −40 °C to 90 °C. Transient frequency of

TABLE I
MEASUREMENT SUMMARY AND COMPARISON WITH PRIOR ART

	[16]	[15]	[8]	[22]	[19]	[17]	[18]	This Work
CMOS process (nm)	180	65	90	65	65	65	55	180
Core area (mm^2)	0.12	0.08	0.072	0.023	0.09	0.069	0.049	0.108
Supply (V)	1.5	1.68	1	0.35	1	1	1.2	1
Frequency (MHz)	39.25	24	24	24	50	54	32	48
Load capacitor C_L (pF)	6	6	10	6	9	6	6	8
Steady-state amplitude (V)	1.5	N/A	N/A	0.3	0.2[2]	0.7	0.37	0.7
Phase noise (dBc/Hz) at 1 kHz	-147	N/A	N/A	-134	N/A	-139.5	N/A	-135
Steady-state power (μW)[1]	181	393	95	31.8	195	198	190	180
Start-up time T_S (μs)	158	64	200	400	2.2[2]	19	23	18
T_S improvement ratio	13.3×	6.7×	13.3×	3.3×	N/A	31.5×	17.4×	102.7×
Start-up energy E_S (nJ)	349	N/A	36	14.2	13.3[2]	34.9	20.2	114.5
E_S improvement ratio	1.1×	N/A	6.9×	2.8×	N/A	N/A	N/A	2.9×
ΔT_S over Temp. (%)	7	±35	27.5	7.5	7	±1.25	±10	±12
Temp. range (°C)	-30 to 125	-40 to 90	-40 to 90	-40 to 90	-40 to 90	-40 to 85	-40 to 140	-40 to 90
Start-up technique	Chirp injection g_m boost	Dithered injection	Dynamic load, g_m boost	3-stage g_m, Chirp injection	Precisely-timed injection	2-step injection	Synchronized signal injection	PDI, AI

ECS-33B SMD crystal is used.

[1] Heavily depends on frequency, supply, C_L, crystal properties and steady-state amplitude.

[2] Steady-state amplitude is limited to ∼0.2V by a regulation loop, requiring only an external injection for a very short time.

XO during start-up settles within ±20 ppm of its steady state in <18 μs, as shown in Fig. 23. Fig. 24 shows the measured phase noise profile of the XO, where a −135-dB/Hz phase noise at 1-kHz offset is reported. Spurious tones seen on the profile are due to weak supply bypass capacitors on board. Table I summarizes the performance of the XO using the proposed techniques in comparison with prior work. To better assess the effectiveness of various start-up techniques, both C_L and the steady-state amplitude that is proportional to the square root of crystal energy should be taken into consideration [see (8)] and are, thus, included in Table I. This paper achieves the largest T_S improvement ratio to date while maintaining an E_S improvement ratio compared with the prior art.

VI. CONCLUSION

This paper presented a study and design of two techniques used to reduce start-up time (T_S) and energy (E_S) of the Pierce crystal oscillator (XO). An analytical study of the external signal injection was presented, and an RXO was proposed as an alternative external injection source to minimize T_S. An overview of limitation imposed by the crystal's static capacitor on XO start-up time was presented, and an AI was designed to mitigate its effects. The simulation and measurement results of a prototype in a 180-nm CMOS process verified the efficacy of the proposed techniques. A significant increase in T_S improvement ratio was achieved across a wide temperature range.

ACKNOWLEDGMENT

The authors would like to thank Keysight Technologies (especially D. Huh) for providing measurement equipment.

REFERENCES

[1] M. R. Palattella, N. Accettura, L. A. Grieco, G. Boggia, M. Dohler, and T. Engel, "On optimal scheduling in duty-cycled industrial IoT applications using IEEE802.15.4e TSCH," *IEEE Sensors J.*, vol. 13, no. 10, pp. 3655–3666, Oct. 2013.

[2] N. Choudhury, R. Matam, M. Mukherjee, and L. Shu, "Beacon synchronization and duty-cycling in IEEE 802.15.4 cluster-tree networks: A review," *IEEE Internet Things J.*, vol. 5, no. 3, pp. 1765–1788, Jun. 2018.

[3] R. C. Carrano, D. Passos, L. C. S. Magalhaes, and C. V. N. Albuquerque, "Survey and taxonomy of duty cycling mechanisms in wireless sensor networks," *IEEE Commun. Surveys Tuts.*, vol. 16, no. 1, pp. 181–194, 1st Quart., 2014.

[4] J. Pandey, J. Shi, and B. Otis, "A 120μw MICS/ISM-band FSK receiver with a 44μW low-power mode based on injection-locking and 9× frequency multiplication," in *IEEE Int. Solid-State Circuits Conf. Dig. Tech. Papers*, Feb. 2011, pp. 460–462.

[5] S. Iguchi, T. Sakurai, and M. Takamiya, "A low-power CMOS crystal oscillator using a stacked-amplifier architecture," *IEEE J. Solid-State Circuits*, vol. 52, no. 11, pp. 3006–3017, Nov. 2017.

[6] S. Iguchi, A. Saito, Y. Zheng, K. Watanabe, T. Sakurai, and M. Takamiya, "93% power reduction by automatic self power gating (ASPG) and multistage inverter for negative resistance (MINR) in 0.7V, 9.2 μW, 39 MHz crystal oscillator," in *IEEE Symp. VLSI Circuits Dig. Tech. Papers*, Jun. 2013, pp. C142–C143.

[7] G. P. Schwieterman, K. E. Jackoski, and J. W. Simmons, "Method and apparatus for optimizing an oscillator start up time," U.S. Patent 5 844 448, Dec. 1, 1998. [Online]. Available: https://patents.google.com/patent/US5844448A/en?oq=5%2c844%2c448

[8] M. Ding *et al.*, "A 95 μW 24 MHz digitally controlled crystal oscillator for IoT applications with 36nJ start-up energy and >13× start-up time reduction using a fully-autonomous dynamically-adjusted load," in *IEEE Int. Solid-State Circuits Conf. (ISSCC) Dig. Tech. Papers*, Feb. 2017, pp. 90–91.

[9] K. L. F. I-Chang Wu and C. W. Lo, "Method and apparatus for a crystal oscillator to achieve fast start-up time, low power and frequency calibration," U.S. Patent 7 348 861 B1, Mar. 25, 2008. [Online]. Available: https://patents.google.com/patent/US7348861B1/en?oq=7%2c348%2c861

[10] T. D. Davis, "Pierce crystal oscillator having reliable startup for integrated circuits," U.S. Patent 5 528 201 A, Jun., 1996. [Online]. Available: https://patentimages.storage.googleapis.com/73/91/9b/4fa947e7131ebb/US5%528201.pdf

[11] K.-M. Lei, P.-I. Mak, and R. P. Martins, "A 0.4V 4.8μw 16 MHz CMOS crystal oscillator achieving 74-fold startup-time reduction using momentary detuning," in *Proc. IEEE Int. Symp. Circuits Syst. (ISCAS)*, May 2017, pp. 1–4.

[12] K.-M. Lei, P.-I. Mak, M.-K. Law, and R. P. Martins, "A regulation-free sub-0.5-V 16-/24-MHz crystal oscillator with 14.2-nJ startup energy and 31.8-μW steady-state power," *IEEE J. Solid-State Circuits*, vol. 53, no. 9, pp. 2624–2635, Sep. 2018.

[13] B. Kleveland, "Fast startup resonant element oscillator," U.S. Patent 2009 0015342 A1, Jan. 15, 2009. [Online]. Available: https://patents.google.com/patent/US20090015342A1/en?oq=US+2009%2f00153%42+A1

[14] Y. I. Kwon, S.-G. Park, T.-J. Park, K.-S. Cho, and H.-Y. Lee, "An ultra low-power CMOS transceiver using various low-power techniques for LR-WPAN applications," *IEEE Trans. Circuits Syst. I, Reg. Papers*, vol. 59, no. 2, pp. 324–336, Feb. 2012.

[15] D. Griffith, J. Murdock, and P. T. Røine, "A 24 MHz crystal oscillator with robust fast start-up using dithered injection," in *IEEE Int. Solid-State Circuits Conf. (ISSCC) Dig. Tech. Papers*, Jan./Feb. 2016, pp. 104–105.

[16] S. Iguchi, H. Fuketa, T. Sakurai, and M. Takamiya, "Variation-tolerant quick-start-up CMOS crystal oscillator with chirp injection and negative resistance booster," *IEEE J. Solid-State Circuits*, vol. 51, no. 2, pp. 496–508, Feb. 2016.

[17] K. M. Megawer *et al.*, "A 54 MHz crystal oscillator with 30× start-up time reduction using 2-step injection in 65 nm CMOS," in *IEEE Int. Solid-State Circuits Conf. (ISSCC) Dig. Tech. Papers*, Feb. 2019, pp. 302–304.

[18] B. Verhoef, J. Prummel, W. Kruiskamp, and R. Post, "A 32 MHz crystal oscillator with fast start-up using synchronized signal injection," in *IEEE Int. Solid-State Circuits Conf. (ISSCC) Dig. Tech. Papers*, Feb. 2019, pp. 304–305.

[19] H. Esmaeelzadeh and S. Pamarti, "A quick startup technique for high-Q oscillators using precisely timed energy injection," *IEEE J. Solid-State Circuits*, vol. 53, no. 3, pp. 692–702, Mar. 2018.

[20] E. Vittoz, *Low-Power Crystal and MEMS Oscillators*, 1st ed. New York, NY, USA: Springer, 2010.

[21] H. Esmaeelzadeh and S. Pamarti, "A precisely-timed energy injection technique achieving 58/10/2μs start-up in 1.84/10/50 MHz crystal oscillators," in *Proc. IEEE Custom Integr. Circuits Conf.*, Apr./May 2017, pp. 1–4.

[22] K.-M. Lei, P.-I. Mak, M.-K. Law, and R. P. Martins, "A regulation-free sub-0.5V 16/24 MHz crystal oscillator for energy-harvesting BLE radios with 14.2nJ startup energy and 31.8pW steady-state power," in *IEEE Int. Solid-State Circuits Conf. (ISSCC) Dig. Tech. Papers*, Feb. 2018, pp. 52–54.

[23] Y. Tokunaga, S. Sakiyama, A. Matsumoto, and S. Dosho, "An on-chip CMOS relaxation oscillator with voltage averaging feedback," *IEEE J. Solid-State Circuits*, vol. 45, no. 6, pp. 1150–1158, Jun. 2010.

[24] *The Quartz Crystal Model and Its Frequencies*. Accessed: Feb. 2019. [Online]. Available: http://statek.com/wp-content/uploads/2018/03/tn32.pdf

Alireza Karimi-Bidhendi (S'15) received the B.Sc. degree from the Sharif University of Technology, Tehran, Iran, in 2013, and the M.Sc. and Ph.D. degrees from the University of California at Irvine, Irvine, CA, USA, in 2018 and 2019, respectively, all in electrical engineering.

In 2015 and 2016, he was with Indie Semiconductor, Aliso Viejo, CA, USA, as an Engineering Intern, working on low-power oscillators and analog-to-digital converters. His research interests include analog, RF, and mixed-signal circuit design for biomedical applications.

Dr. Karimi-Bidhendi is a Student Member of the IEEE Solid-State Circuits Society and the IEEE Circuits and Systems Society. He was a recipient of the 2013–2014 Departmental Fellowship and the 2014 Henry Samueli Fellowship. He has served as a Reviewer for the IEEE TRANSACTIONS ON CIRCUITS AND SYSTEMS I AND II, the IEEE Biomedical Circuits and Systems Conference, the IEEE TRANSACTIONS ON BIOMEDICAL CIRCUITS AND SYSTEMS, the IEEE SOLID-STATE CIRCUITS LETTERS, the IEEE International Solid-State Circuits Conference, and the IEEE International Symposium on Circuits and Systems.

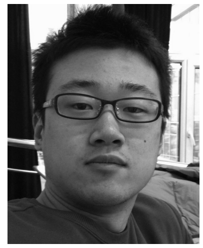

Haoran Pu (S'18) received the B.S. degree (Hons.) in electrical and computer engineering from The Ohio State University, Columbus, OH, USA, in 2015, and the M.S. degree in electrical engineering from the University of California at San Diego (UCSD), La Jolla, CA, USA, in 2017. He is currently pursuing the Ph.D. degree in electrical engineering with the University of California at Irvine (UCI), Irvine, CA, USA.

In 2018, he was with Broadcom Inc., San Diego, CA, USA, where he worked on power detectors for CMOS power amplifiers. His current research focuses on low-power biomedical integrated circuits for brain–computer interfaces.

Mr. Pu was a recipient of the UCI Henry Samueli School of Engineering Fellowship in 2017.

Payam Heydari (M'01–SM'09–F'17) received the B.S. and M.S. degrees (Hons.) in electrical engineering from the Sharif University of Technology, Tehran, Iran, in 1992 and 1995, respectively, and the Ph.D. degree from the University of Southern California, Los Angeles, CA, USA, in 2001.

He is currently a Full Professor of electrical engineering with the University of California at Irvine, Irvine, CA, USA, where he is also the Director of Nanoscale Communication IC (NCIC) Labs. He has (co)-authored two books, one book chapter, and more than 150 journal and conference papers. His research covers the design of terahertz/millimeter-wave/RF and analog integrated circuits.

Dr. Heydari was a member of the Technical Program Committee of the International Solid-State Circuits Conference. He is a Technical Program Committee Member of the IEEE Custom Integrated Circuits Conference. He is an AdCom Member of the IEEE Solid-State Circuits Society. He was a recipient of the 2016–2017 UCI's School of Engineering Mid-Career Excellence in Research, the 2014 Distinguished Engineering Educator Award from the Orange County Engineering Council, the 2009 Business Plan Competition First Place Prize Award and the Best Concept Paper Award both from the Paul Merage School of Business at UC-Irvine, the 2010 Faculty of the Year Award from the UC-Irvine's Engineering Student Council (ECS), the 2009 School of Engineering Best Faculty Research Award, the 2007 IEEE Circuits and Systems Society Guillemin-Cauer Award, the 2005 IEEE Circuits and Systems Society Darlington Award, the 2005 National Science Foundation (NSF) CAREER Award, the 2005 Henry Samueli School of Engineering Teaching Excellence Award, the Best Paper Award at the 2000 IEEE International Conference on Computer Design (ICCD), and the 2001 Technical Excellence Award from the Association of Professors and Scholars of Iranian Heritage (APSIH). He was recognized as the 2004 Outstanding Faculty at the EECS Department, University of California at Irvine. His research on novel low-power multi-purpose multi-antenna RF front-ends received the Low-Power Design Contest Award at the 2008 IEEE International Symposium on Low-Power Electronics and Design (ISLPED). He gave a keynote speech to the IEEE GlobalSIP 2013 Symposium on Millimeter Wave Imaging and Communications, served as an Invited Distinguished Speaker for the 2014 IEEE Midwest Symposium on Circuits and Systems, and gave a tutorial at the 2017 International Solid-State Circuits Conference. He was a Distinguished Lecturer of the IEEE Solid-State Circuits Society from 2014 to 2016. He has been a Distinguished Microwave Lecturer of the IEEE Microwave Theory and Techniques Society since 2019. His group was among the first who introduced the design of millimeter-wave integrated circuits in silicon technologies. They demonstrated the world's first fundamental frequency CMOS transceiver operating above 200 GHz, the world's highest radiated power and highest efficiency sub-terahertz circularly polarized radiator in silicon employing a multi-port cavity-backed structure. He was an Associate Editor of the IEEE TRANSACTIONS ON CIRCUITS AND SYSTEMS I. He currently serves both as an Associate Editor and a Guest Editor for the IEEE JOURNAL OF SOLID-STATE CIRCUITS and an Associate Editor for the IEEE SOLID-STATE CIRCUITS LETTERS.